Evidence for Dissociation in Shock-Compressed Methane

G. Tabak,[1,2] J. R. Rygg,[1,3,2] M. Millot,[4] Y.-J. Kim,[4] S. Hamel,[4] P. M. Celliers,[4] D. E. Fratanduono,[4] S. Ali,[4] D. Erskine,[4] T. R. Boehly,[1] N. Dasenbrock-Gammon,[2] R. Dias,[3,2] T.-A. Suer,[1] S. Zhang,[1] S. X. Hu,[1,3,2] L. E. Hansen,[1,2] B. J. Henderson,[1,2] M. Zaghoo,[1] T. Ogawa,[5] D. Murayama,[5] K. Miyanishi,[5,6] N. Ozaki,[5,7] T. Sano,[5,7] R. Jeanloz,[8] D. G. Hicks,[9] J. H. Eggert,[4] and G. W. Collins[1,3,2]

[1]*Laboratory for Laser Energetics, Rochester, New York 14623, USA*
[2]*Department of Physics and Astronomy, University of Rochester, Rochester, New York 14611, USA*
[3]*Department of Mechanical Engineering, University of Rochester, Rochester, New York 14611, USA*
[4]*Lawrence Livermore National Laboratory, Livermore, California 94550-9234, USA*
[5]*Graduate School of Engineering, Osaka University, Suita, Osaka 565-0871, Japan*
[6]*RIKEN SPring-8 Center, Hyogo 679-5148, Japan*
[7]*Institute of Laser Engineering, Osaka University, Suita, Osaka 565-0871, Japan*
[8]*Department of Earth and Planetary Science,*
University of California Berkeley, Berkeley, CA 94720, USA
[9]*Optical Sciences Centre, Department of Physics and Astronomy,*
Swinburne University of Technology, Hawthorn, Victoria 3122, Australia

(Dated: August 18, 2023)

Theory and experiments show that with increasing pressure, the chemical bonds of methane rearrange, leading to the formation of complex polymers and then to dissociation. However, there is disagreement on the exact conditions where these changes take place. In this study, methane samples were precompressed in diamond-anvil cells and then shock compressed to pressures reaching 400 GPa, the highest pressures yet explored in methane. The results reveal a qualitative change in the Hugoniot curve at 80-150 GPa, which is interpreted as a signature of dissociation based on thermodynamic calculations and theoretical predictions.

I. INTRODUCTION

The carbon-hydrogen system is important to high energy density physics in both pure and applied contexts. For example, methane (CH_4) is expected to exist at extreme conditions in the interiors of giant planets such as Uranus and Neptune. These planets are thought to contain an outer hydrogen-helium layer, a central ice layer of water, methane, and ammonia at pressure-temperature conditions of several 100 GPa and ~3000-6000 K, and a rocky core [1–3]. An experimentally informed equation of state (EOS) for the constituents of the central ice layer enables accurate density profiles and mass-radius relations for giant planets. This can help elucidate experimental measurements of gravitational fields for the solar system gas giants [2, 3] and also connects with comprehensive studies of the growing number of discovered exoplanets [4]. Hydrocarbon plastics such as polystyrene (CH) and polypropylene (CH_2) are routinely used as ablator materials in dynamic compression experiments, including inertial confinement fusion targets. Thus, the high pressure behavior of methane can aid in understanding the effect of C:H composition on the performance of various ablators [5].

Experimental and theoretical evidence suggests that the properties of methane are complex at pressures up to and exceeding 100 GPa. Diamond-anvil cell (DAC) EOS measurements on methane at 300 K and pressures up to 200 GPa have revealed multiple solid phases [6]; theoretical studies at similar temperatures [7, 8] predict a gradual sequence of bonding changes and ultimate decomposition into carbon and hydrogen. Gradual polymerization and decomposition is also predicted at higher temperatures of 1000 to 4000 K; the decomposition pressure increases with decreasing temperature to near 300 GPa at temperatures below 500 K [7–10]. A comprehensive theoretical study shows that diamond formation in hydrocarbons is favorable above 200 GPa and below 3000 to 3500 K regardless of the C:H ratio [11]. Polymerization has been observed in laser heated diamond-anvil cell experiments on methane at 1000 to 3000 K and 10 to 80 GPa, with diamond formation occurring by 3000 K [12, 13]. Shock compression simulations on methane suggest that polymerization can occur under dynamic compression [14]. Prior shock compression data on CH_4 are limited to pressures below 100 GPa, starting from the cryogenic liquid initial density (0.42 g/cm^3), and reach temperatures of several 1000 K [15, 16]. In contrast to the static experiments and the more recent theoretical works, the earlier gas-gun data have been fit with a mixing model and interpreted as showing evidence of dissociation into hydrogen and diamond particles by 10 GPa and 1000 K [15]. DC conductivity measurements on shocked cryogenic samples [16] indicate that the methane molecules decompose with increasing pressure, leading to a substantial free carrier population by 36 GPa. Another comprehensive theoretical study on hydrocarbons [17, 18] indicates that linear mixing of pure carbon and pure hydrogen reasonably describes the EOS of high-pressure hydrocarbon mixtures at temperatures above 5,000 K.

This work describes new shock compression experiments on methane samples precompressed in diamond-anvil cells, reaching pressures near 400 GPa. The combination of static compression in DACs with dynamic compression by laser-driven shocks [19] enables the study of a broad range of high-pressure conditions and has already been used to investigate other materials [20–28]. The DACs can vary the initial density of the sample, granting access to a wider range of conditions. This paper is organized as follows. In Sec. II, we give an overview of the experimental method, in Sec. III we present the results and discussion, and the conclusions are given in Sec. IV.

II. EXPERIMENTAL METHOD

The methane targets were precompressed in DACs to a range of densities from those previously achieved with cryogenic samples (0.42 g/cm^3 at 111 K) to ∼0.56 g/cm^3 (corresponding to static pressures of 0.3-1 GPa). The DACs used two opposing diamond anvils with small tips of diameter ∼700 μm to compress the samples (Fig. 1(a)). Some targets used a sapphire anvil on one side. The laser side diamond anvil was coated with gold and CH plastic to serve as an X-ray shield and ablator, respectively. The opposite window anvil had antireflective coatings designed for 532 nm to facilitate the optical measurements of the shocked sample. An annular stainless steel gasket confined the sample between the small tips of the anvils. A quartz plate was attached to the laser drive side anvil inside the chamber to be used as an impedance matching standard for shock measurements [24, 29–32].

While optical techniques were used to directly measure the sample pressure and thickness [33–35], the initial density, refractive index, and sound speed were determined by fitting existing data on these parameters (Equation (1)). Thermodynamic data on methane were obtained using the program REFPROP [36–38] and then used to fit the density ρ and the sound speed C_s of methane as a function of pressure P. The refractive index was fit as a function of density using cryogenic measurements of the refractive index of saturated liquid methane [39]. DAC measurements of the refractive index at higher fluid densities have also been performed [40, 41]; however, these data are less precise and therefore were not used in the fit (see Appendix). The functional forms used for these fits are given in Equation (1), and the fit parameters are given in Table I the Appendix. The functional forms are

$$\begin{aligned} \rho(P) &= a_1(a_2(P-P_\mathrm{ref})+1)^{a_3}, \\ n &= c_1\rho + c_0, \\ C_s &= b_2\rho^2 + b_1\rho + b_0. \end{aligned} \tag{1}$$

The high-power laser facilities Omega (Laboratory for Laser Energetics, Rochester, NY) and GEKKO-XII (Osaka University, Osaka, Japan) were used to drive shock waves through the targets, compressing the methane up to 400 GPa. The drive lasers ablated the plastic coating on the drive side diamond, launching a shock wave that traveled through the diamond and into the sample chamber, where the quartz and methane became reflective at the shock front. Velocity interferometry (VISAR) was used to track the velocity of the reflective shock front throughout the experiment [42, 43], made possible by the transparent anvil opposite the laser drive (on the right in Fig. 1(a)). VISAR recorded the Doppler shift of a 532 nm probe laser that reflected off the moving shock front to measure the shock velocity. The interference fringes were recorded over the duration of the experiment on a streak camera to provide a time history of the shock as it traversed the precompressed sample (Fig. 1(b)). For VISAR measurements of a reflective shock in an optically dense medium, it is necessary to divide the apparent (measured) velocity by the refractive index of the unshocked medium [42] and the refractive index fit for methane was used for this purpose. The antireflective coatings on the window anvil served to minimize background reflections and a previously developed algorithm was used to subtract the resultant weak background fringes [44].

The pressure, density, and internal energy for shock compressed methane were determined using the Rankine-Hugoniot equations [45],

$$\begin{aligned} \rho_0 U_s &= \rho_1(U_s - U_p), \\ P_1 - P_0 &= \rho_0 U_s U_p, \\ E_1 - E_0 &= \frac{1}{2}(P_0 + P_1)(1/\rho_0 - 1/\rho_1), \end{aligned} \tag{2}$$

where ρ, U_s, U_p, P, and E are the density, shock velocity, particle velocity behind the shock front, pressure, and specific internal energy per mass, respectively, and the subscripts 0 and 1 refer to the initial and shocked conditions, respectively. This form of the equations assumes the unshocked material is initially at rest. Given an initial density and pressure, the locus of all states accessible via shock compression is a single curve known as the Hugoniot, defined by these equations. As there are five variables but three equations, two variables need to be determined. We measured the shock velocity in the methane and used impedance matching with quartz [24, 29–32] to infer the particle velocity, which closes the equations (2). As indicated by these equations, the Hugoniot curve is affected by the initial density ρ_0. Precompression in DACs varied the initial density and thus made it possible to span multiple Hugoniot curves.

The error analysis took into account both systematic and random uncertainties. The random uncertainties originated from measurements of pressure in the DACs and velocities derived form VISAR. Systematic uncertainties originated from the models of the density and refractive index of precompressed methane, and the quartz Hugoniot and release. A Monte Carlo routine was implemented to simultaneously account for both systematic and random errors, leading to a result for the uncertainties in the methane shock pressure, shock density, and the other parameters.

III. RESULTS AND DISCUSSION

Changes in the slope or intercept of the Hugoniot in U_s vs. U_p space, made more apparent by plotting $U_s - U_p$, are typically signatures of a microscopic change in the material. Such a change has been observed to coincide with melting in SiO_2 [29, 30], with the dissociation of hydrogen [20, 24], and with microscopic changes in carbon dioxide [25] and nitrogen [27]. The gas-gun shock wave data on methane at the cryogenic initial density [15] were interpreted as showing a small deviation from linear behavior at significantly lower pressures than those explored here and assuming a constant U_s vs. U_p slope by 40 GPa. Our data (Figs. 2 and 3) are inconsistent with a global linear behavior in U_s vs. U_p, indicating that the Hugoniot traverses a potentially rich phase diagram. Since the shock velocity approaches the isentropic sound speed at the initial density of the Hugoniot curve at arbitrarily low shock pressures [45], sound-speed data on methane [36, 37] are plotted to suggest the limiting value of U_s as $U_p \to 0$.

The gas-gun data and the new laser shock data of this work altogether are fit with a new piecewise function to account for the observed changes in the U_s vs. U_p relation. The data at lower pressures are fit with a quadratic relation in U_s vs. U_p while at higher pressures a constant slope is assumed. Fitting a single linear region or two linear regions yielded a significantly worse reduced chi-squared. The boundary between the two regions is determined by enforcing continuity, leading to a breakpoint of $U_{p,\mathrm{lim}} = 11.35$ km/s. At the highest pressures the slope is found to be 1.36, which is close to the analogous values for SiO_2 [29] and CO_2 [25] in the several 100 GPa range. Similar to other materials, [24, 25, 27] incorporating a uniform initial density adjustment based on the sound speed (Equation (1)) yields a reasonable fit to the data, i.e. the Hugoniot relation $U_s(U_p, \rho_0)$ incorporates the term $C_\mathrm{s}(\rho_0) - C_\mathrm{s}(\rho_{0,\mathrm{cryo}})$, which is a function of the initial density:

$$U_s = \begin{cases} B_1 U_p^2 + B_2 U_p + B_3 & \\ +C_\mathrm{s}(\rho_0) - C_\mathrm{s}(\rho_{0,\mathrm{cryo}}) & U_p \leq U_{p,\mathrm{lim}}, \\ SU_p + C & \\ +C_\mathrm{s}(\rho_0) - C_\mathrm{s}(\rho_{0,\mathrm{cryo}}) & U_p > U_{p,\mathrm{lim}}, \end{cases} \tag{3}$$

where $\rho_{0,\mathrm{cryo}} = 0.42$ g/cm^3 is the cryogenic liquid density and ρ_0 is the initial density. The values of the parameters are given in the Appendix. The uncertainties of the sound speed fit are insignificant compared to the measurement uncertainties, so the nominal sound speed fit is used. If the values of U_s are shifted downward by the precompression offset term (Fig. 2(c)), the data collapse into a single curve as expected.

When the data are plotted in pressure vs. compression ratio space (Fig. 3), it is apparent that the compression changes more slowly with increasing pressure at the high pressure limit defined by the breakpoint of $U_{p,\mathrm{lim}} = 11.35$ km/s or 80-100 GPa. While the fit indicates a sharp transition between the two regimes, this is solely based on imposing continuity as there are insufficient data to more precisely constrain the Hugoniot near the breakpoint U_p value.

In the 100 to 400 GPa range methane is more compressible than the plastics polystyrene (CH) [5, 46–49] and polypropylene (CH_2) [5, 49] and shows a much more sudden change in the compression ρ_1/ρ_0 at a critical pressure range, whereas the Hugoniot data on plastics show a more gradual rise in the compression ratio (Fig. 3). The comparably slow density increase with pressure along the Hugoniot curves of the plastics is likely a result of the higher initial densities of the latter compared to those of methane. Similarly, methane itself experiences a more gradual rise in the compression ratio at higher initial densities.

The shock data obtained here are consistent with the pressure-density Hugoniot response predicted by recent DFT-MD (density functional theory molecular dynamics) simulations on methane [10] (Figs. 2-3), which indicate that with increasing shock pressure, methane will first transition to a polymeric regime and eventually fully dissociate into a dense plasma of carbon and hydrogen. The onset of full dissociation occurs near the breakpoint of the U_s vs.

U_p fit (U_p = 11.35 km/s). While both Ref. [10] and Refs. [17, 18, 50] used DFT-MD, there is a significant difference in their predicted behavior of methane at shock pressures above 80 GPa (Figs. 2-3). As finite size effects on simulation precision are well known [17], the better agreement of Ref. [10] with the data may be due to the larger number of nuclei simulated (135 in Ref. [10] vs. 50 in Refs. [17, 18, 50]). The SESAME 5500 Hugoniot curves [51] diverge from the data above 80 GPa (Fig. 2(c)), which is expected as this model does not take dissociation into account.

In addition, the change in specific internal energy as given by the third Hugoniot equation (Equation (2)), can be compared to the enthalpy of breaking a single bond of the CH_4 molecule, $E_{d,1}$=27 MJ/kg, and to the entahlpy of breaking all four bonds, $E_{d,4}$=104 MJ/kg, based on theoretical calculations [52]. The breakpoint of the Hugoniot fit occurs in between these two thresholds (Figs. 2-3), supporting the notion that changes in bonding and dissociation are taking place in this pressure range.

The specific Gibbs free energy, given by

$$G = E + PV - TS \tag{4}$$

where E, P, V, T, S are the specific internal energy, pressure, specific volume, temperature, and specific entropy, respectively, is computed along the Hugoniot to investigate the plausibility of dissociation. E, P, and V can be computed immediately from the Hugoniot equations. Graphically, the energy Hugoniot equation states that the change in internal energy is equal to the area, in pressure-volume space, under the straight line connecting the initial and final states, known as the Rayleigh line. The change in (TS) from shock compression is the pressure-volume integral between the Rayleigh line and the isentrope, and here it is estimated as the pressure-volume integral between the Rayleigh line and a fit to 300 K static data from Ref. [8]. Thus, the change in $E-TS$ along the Hugoniot is approximated as the pressure-volume work along the 300 K isotherm to the same density as that obtained under the shock. The pressure-volume integral under the isotherm is a slight underestimate of the integral for the isentrope. Assuming the isentrope does not rise past 1000 K along the specific volumes of interest, and taking the specific heat to be $3k$ per methane molecule (where k is Boltzmann's constant), the error from the estimate is $\sim$ 1 MJ/kg, which is very small relative to the changes in G considered here.

A simple comparison of the nominal bond enthalpies of methane $E_{d,1}$ and $E_{d,4}$ to the change in Gibbs free energy suggests (Fig. 4) that shock compression provides enough free energy to break the four C-H bonds of the methane molecule near U_p = 14.38 km/s, slightly above the onset of the high-pressure U_s vs. U_p regime. Moreover, a comparison to the change in internal energy shows that at similar values of U_p, the internal energy input from shock compression is comparable to the energy density of the chemical bonds of methane. Thus, there is strong evidence of significant dissociation taking place by $U_p \sim 11.35 - 14.38$ km/s, though the data do not rule out the possibility of lingering chemical bonds in this high pressure regime.

The nonlinear shock velocity-particle velocity response of methane at low pressures suggests the presence of a complex fluid (Fig. 2) where significant chemical bonds are present and that the nature of the bonds changes along the Hugoniot, while the high-pressure region of constant slope corresponds to significant dissociation. The energy change along the Hugoniot is comparable to the enthalpy $E_{d,1}$ of breaking a single C-H bond in CH_4 at $U_p \sim 7.25$ km/s and the enthalpy of breaking all four bonds, $E_{d,4}$ at $U_p \sim 14.38$ km/s. These thresholds are slightly below and above the breakpoint of U_p = 11.35 km/s, respectively. While the reference enthalpy values are based on calculations for low pressure conditions, at elevated pressures less energy may be required to fully dissociate the methane molecule. The location of $E_{d,1}$ below the breakpoint supports the notion that partial dissociation or bonding rearrangements account for the gradual change in the U_s vs. U_p slope at low pressure.

DC conductivity measurements on shocked methane between 20 and 40 GPa [16] support the notion of a gradual chemical rearrangement of CH_4. A mixing model for the conductivity measurements that assumes full dissociation overestimated the measured conductivity in methane at the lowest pressure studied and approached the measurements with increasing pressure, suggesting that hydrogen is incrementally liberated along the Hugoniot [16]. This is consistent with the interpretation of the new data in this work, which indicates a transition to polymers and subsequent dissociation at 80 to 150 GPa based on comparisons with DFT-MD and thermodynamic estimates.

IV. CONCLUSION

The data presented here reveal the complex behavior of methane at extreme conditions. These data provide the first shock measurements on methane above 100 GPa and go up to 400 GPa, a pressure range important for understanding planetary interiors and hydrocarbon ablators. Qualitative changes in the Hugoniot shock velocity-particle velocity response can be seen in the 0 to 150 GPa range. The data are consistent with recent DFT-MD simulations which predict that the phase diagram of methane at these pressures, rather than being a single carbon-hydrogen plasma phase, also includes a polymeric regime at intermediate pressures and temperatures. The data provide evidence that while the methane in the uppermost layers of giant planets retains its chemical bonds, at sufficiently high pressures the methane molecule should dissociate, in accord with theoretical predictions.

ACKNOWLEDGMENTS

This material is based upon work supported by the Department of Energy National Nuclear Security Administration under Award Number DE-NA0003856, the University of Rochester, and the New York State Energy Research and Development Authority. Funding for this research was provided by the Center for Matter at Atomic Pressures (CMAP), a National Science Foundation (NSF) Physics Frontiers Center, under Award PHY2020249. Part of this work was conducted under the joint research of the Institute of Laser Engineering, Osaka University, Japan. This material is partially supported by the Department of Energy, Office of Science, Fusion Energy Sciences under Award No. DE-SC0020340. Part of this work was performed under the auspices of the US Department of Energy by Lawrence Livermore National Laboratory under contract DE-AC52-07NA27344. Part of this work was supported by LLNL LDRD Program No. 19-ERD-031. The VISAR data in this work were analyzed with the LLNL AnalyzeVISAR code. Part of this work was performed as part of the Japan/U.S. Cooperation in Fusion Research and Development.

APPENDIX

Fits for Pressure, Density, and Sound Speed

Plots of the fits for the density ρ, refractive index n, and sound speed C_s for the initial state of methane are given in Figs. 5-7 and the fit parameters are given in Table I. Prior thermodynamic data [36–38] were sampled to extract EOS points giving values for density and sound speed (all at 300 K) at several pressures going up to $P = 1$ GPa. The resulting points were fit to obtain relations for $\rho(P)$ and $C_s(P)$. For the refractive index fit $n(\rho)$, cryogenic data [39] were utilized to obtain a fit for $n(\rho)$. The refractive index fit is plotted in Fig. 6 in comparison with DAC measurements at higher fluid densities [40, 41]. The DAC measurements are less precise than the cryogenic ones and were not used for the fit. As shown in Fig. 6, the DAC measurements are consistent with an extrapolation of the fit to cryogenic data. All the fits are plotted along with their deviation from the underlying data.

Initial state density-pressure fit			
a_1 [g/cm^3]	a_2 [GPa^{-1}]	a_3	P_{ref} [GPa]
0.341	14.3	0.194	0.1
Initial state refractive index fit			
c_1 [cm^3/g]		c_0	
0.684		0.987	
Initial state sound speed fit			
b_2 [$\frac{\text{km-cm}^6}{\text{s-g}^2}$]	b_1 [$\frac{\text{km-cm}^3}{\text{s-g}}$]	b_0 [km/s]	
8.14	1.26	-1.15e-01	

TABLE I. Fit parameters for precompressed methane (eqn. 1). For the density vs. pressure fit, the uncertainty is a systematic error envelope of 0.15%, based on the uncertainty of the REFPROP model [36–38]. This is negligible compared to the effect of the DAC pressure uncertainty. For the refractive index, the random uncertainties of the cryogenic measurements used to construct the fit [39] are also negligible compared to the random errors arising from the DAC pressure measurement. Finally, the nominal fit to the sound speed vs. density relation was taken as the precompression offset in the Hugoniot fit.

Data Table

Table II provides the data for each shot. The facility is identified as either O60 (OMEGA 60, at LLE), EP (OMEGA EP, at LLE) or G (GEKKO-XII, at Osaka University). Uncertainties are given in parentheses. All parameters are for methane except U_s(qtz), which is the shock velocity measured in the quartz. The subscripts 0 and 1 refer to the conditions of the unshocked and shocked state, respectively. Table III provides the target layers of the cell from each shot.

Facility	Shot Number	P_0 [GPa]	ρ_0 [g/cm^3]	U_s(qtz) [km/s]	U_s(CH$_4$) [km/s]	U_p(CH$_4$) [km/s]	ρ_1(CH$_4$) [g/cm^3]	P_1(CH$_4$) [GPa]
O60	64353	0.98(0.03)	0.566(0.004)	24.92(0.09)	31.57(0.11)	22.12(0.58)	1.90(0.12)	397(11)
O60	64356	1.07(0.03)	0.576(0.003)	15.64(0.09)	17.95(0.11)	12.16(0.25)	1.79(0.08)	127(3)
O60	69338	0.3(0.03)	0.443(0.010)	26.79(0.23)	34.50(0.32)	25.35(0.76)	1.69(0.16)	388(13)
O60	69339	0.28(0.03)	0.437(0.010)	22.04(0.23)	27.33(0.31)	19.94(0.56)	1.63(0.15)	238(8)
G	36738	0.45(0.03)	0.483(0.007)	16.50(0.14)	19.16(0.18)	13.51(0.32)	1.65(0.11)	126(4)
EP	33725	0.96(0.08)	0.564(0.009)	17.13(0.10)	20.16(0.15)	13.73(0.29)	1.77(0.09)	157(4)
EP	33727	0.96(0.08)	0.563(0.010)	13.07(0.10)	15.16(0.14)	9.57(0.21)	1.53(0.07)	83(2)
EP	33728	1.04(0.08)	0.573(0.009)	12.41(0.10)	14.53(0.13)	8.89(0.20)	1.48(0.06)	75(2)
EP	33730	0.77(0.08)	0.539(0.011)	17.68(0.10)	20.74(0.16)	14.49(0.32)	1.8(0.11)	163(4)
O60	101059	0.65(0.08)	0.521(0.013)	17.77(0.25)	21.01(0.32)	14.66(0.44)	1.73(0.15)	161(6)

TABLE II. Experimental data for shock compressed methane. The OMEGA 60 and OMEGA EP laser facilities at the Laboratory for Laser Energetics are denoted as O60 and EP, respectively. GEKKO-XII (Osaka University) is denoted as G.

Shot Number	CH	Au	C	Qtz	CH_4	Window
64353	15	2	350	20	150	5000
64356	15	2	350	20	150	5000
69338	10	4	350	16	200	5000
69339	10	4	350	16	150	5000
36738	20	4	200	15	200	5000
33725	25	4	390	30	60	1300
33727	25	4	390	30	85	1300
33728	30	5	390	30	110	1300
33730	25	4	390	30	110	1300
101059	30	4	390	30	100	1300

TABLE III. Specifications for each target. All layer thicknesses are given in μm, starting from the laser side and moving toward the opposite side of the target. Windows with thicknesses below 2000 μm are diamonds, while the 5000 μm windows are sapphires (the anvils on the laser side are always diamonds).

Hugoniot Fit

The Hugoniot fit parameters (with uncertainties given in parentheses) and nonzero covariance matrix elements are given in Table IV. The breakpoint $U_{p,\mathrm{lim}} = 11.35$ km/s is determined by imposing continuity on the fit. The deviations of the shock velocity data from the fit are plotted in Fig. 8.

Hugoniot fit parameters	
B_1 [s/km]	-0.0229(0.00307)
B_2	1.44(0.0338)
B_3	2.09(0.0766)
S	1.36(0.0151)
C [km/s]	0.0782(0.227)
Nonzero covariance matrix elements	
σ_{B_1,B_1}	9.42e-06
σ_{B_2,B_2}	1.44e-03
σ_{B_3,B_3}	5.87e-03
$\sigma_{S,S}$	2.29e-04
$\sigma_{C,C}$	5.15e-02
σ_{B_1,B_2}	-1.03e-04
σ_{B_1,B_3}	2.18e-04
σ_{B_2,B_3}	-2.51e-03
$\sigma_{S,C}$	-3.36e-03

TABLE IV. CH_4 Hugoniot fit parameters and covariance matrix elements.

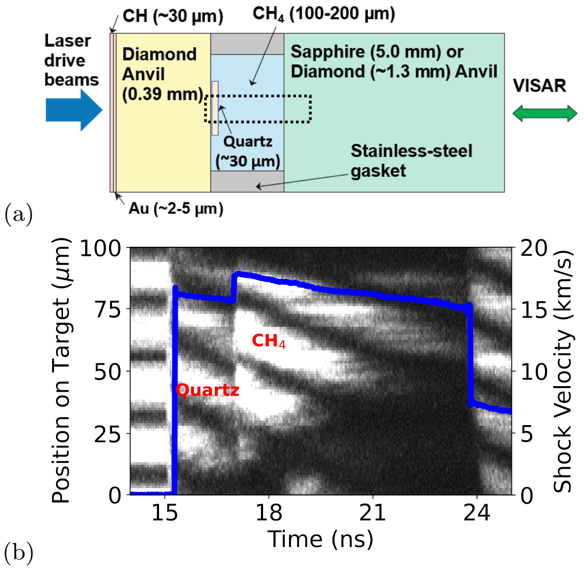

FIG. 1. (a): Diamond-anvil cell target assembly. The drive lasers hit the outer side of the diamond anvil, which is coated with gold and CH plastic, ablating the plastic and driving a shock wave through the diamond anvil and into the sample chamber, while optical diagnostics probe the experiment through the transparent anvil on the right. (b): VISAR streak camera image for Omega 60 shot 64356, and the resulting lineout of shock velocity. The VISAR image was acquired across the spatial extent of the quartz as indicated by the dashed rectangle in (a). The profile at ∼15-24 ns is the measured shock velocity during the transit through the quartz and methane, where the measured apparent velocity was corrected with the refractive index. The profile past ∼ 24 ns is an unused apparent velocity corresponding to the shock traveling through the window anvil.

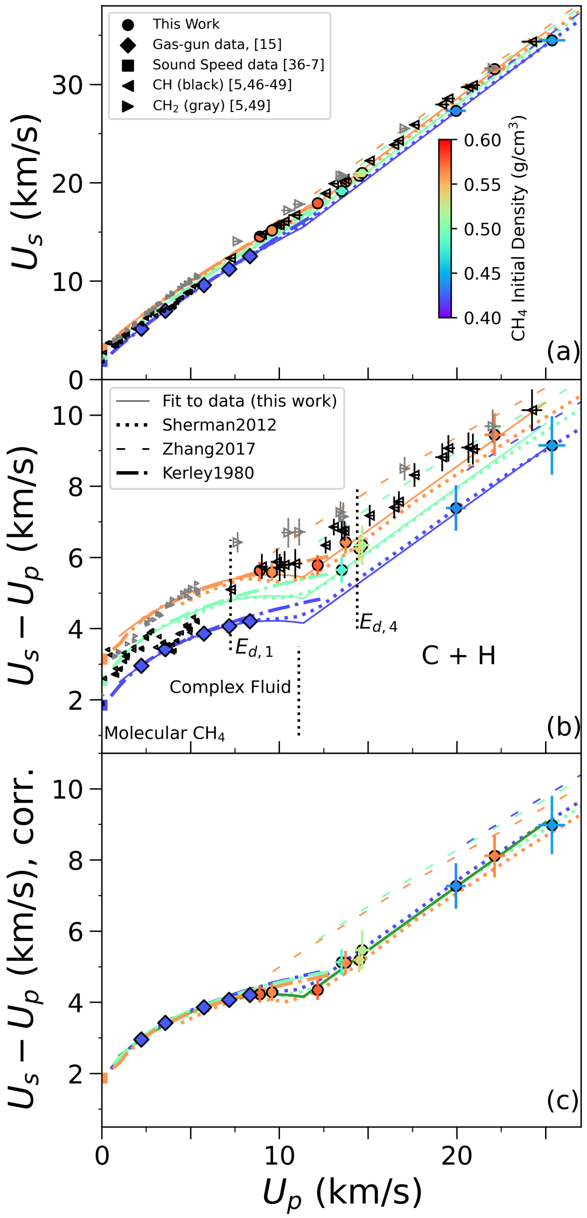

FIG. 2. Shock velocity U_s vs. particle velocity U_p in methane (a). In (b), $U_s - U_p$ is shown. (c) shows the "collapsed" Hugoniot resulting from shifting all the data downward by the precompression offset $C_s(\rho_0) - C_s(\rho_{0,\mathrm{cryo}})$. Gas-gun data are from Ref. [15]. Also shown are DFT-MD simulations from [10] (labeled Sherman2012), the calculations from the FPEOS table for methane (Zhang2017) [17, 18, 50], and SESAME table 5500 for methane (Kerley1980) [51]. Hugoniot curves are plotted for the initial densities 0.42, 0.50, and 0.56 g/cm^3. Sound speed values from Refs. [36, 37] are plotted in squares. The lower black dotted line in (b) demarcates the proposed boundary between a complex fluid at low pressures and the high-pressure regime where there is significant dissociation into carbon and hydrogen. The vertical dotted lines labeled $E_{d,1}$ and $E_{d,4}$ indicate where the Hugoniot energy change corresponds to the enthalpy of dissociation for one (27 MJ/kg) and for all four bonds (104 MJ/kg) of the methane molecule, respectively [52]. Also plotted are shock data on polystyrene (CH) [5, 46–49] and polypropylene (CH_2) [5, 49].

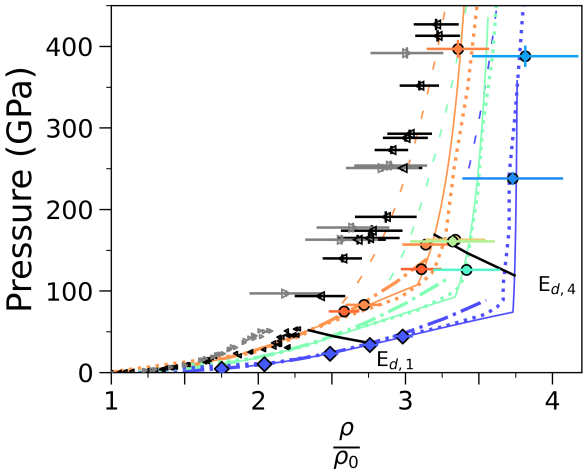

FIG. 3. Pressure vs. compression ratio in methane. Data and curves are as in Fig. 2. The points on the Hugoniot curves (of the fit, shown by solid lines) where the change in internal energy matches the nominal dissociation enthalpy of one or of all four bonds of the methane molecule, $E_{d,1}$ and $E_{d,4}$, are plotted with the solid black lines and correspond to the analogously labeled vertical lines in Fig. 2. The dissociation energies are based on theoretical bond enthalpy values for methane [52].

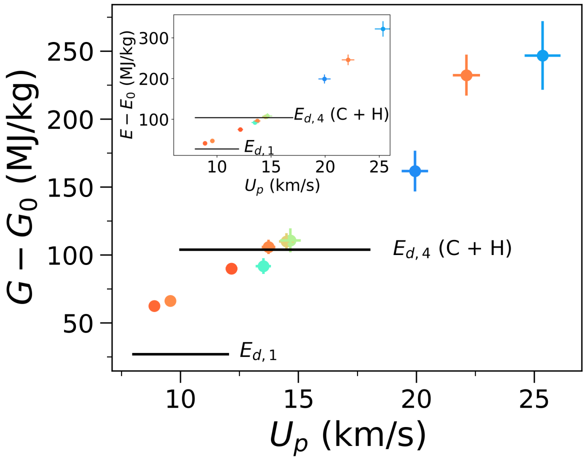

FIG. 4. Change in specific Gibbs free energy under shock compression for methane. Data and color scale are as in the previous figures. Calculations of the bond dissociation enthalpy for methane, based on reference values for methane [52], are shown for comparison as in Figs. 1-2. Inset: change in specific internal energy for methane under shock compression.

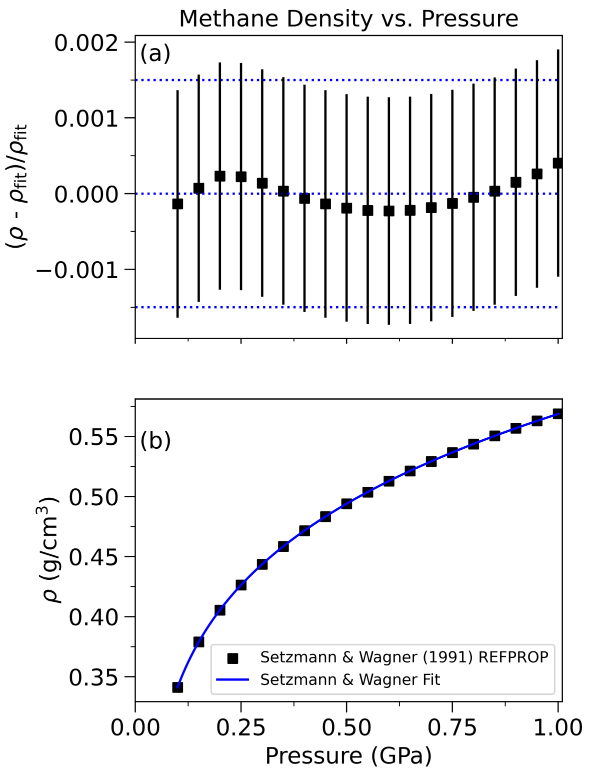

FIG. 5. Density fit for methane. REFPROP [37] was utilized to sample the thermodynamic data of Setzmann and Wagner for methane [36, 38]. The REFPROP model has a systematic uncertainty of 0.15%. (a) Deviation of REFPROP points (black) from fit with error envelope (blue). (b) Methane density vs. pressure.

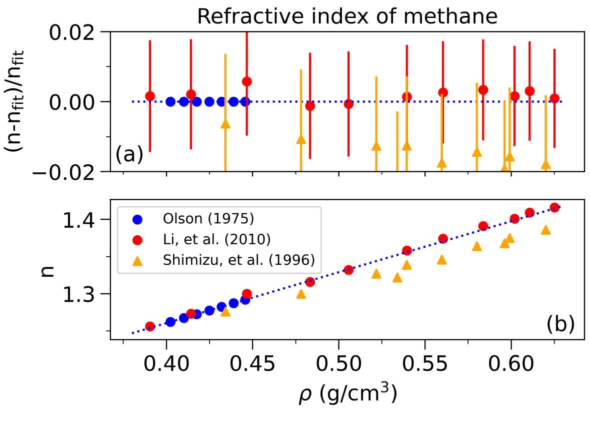

FIG. 6. Refractive Index fit for methane, based on cryogenic data [39] (cryogenic data and fit are in blue). Diamond anvil-cell data on fluid methane [40, 41] are shown for comparison. (a) Deviation of data from fit. (b) Methane refractive index vs. density.

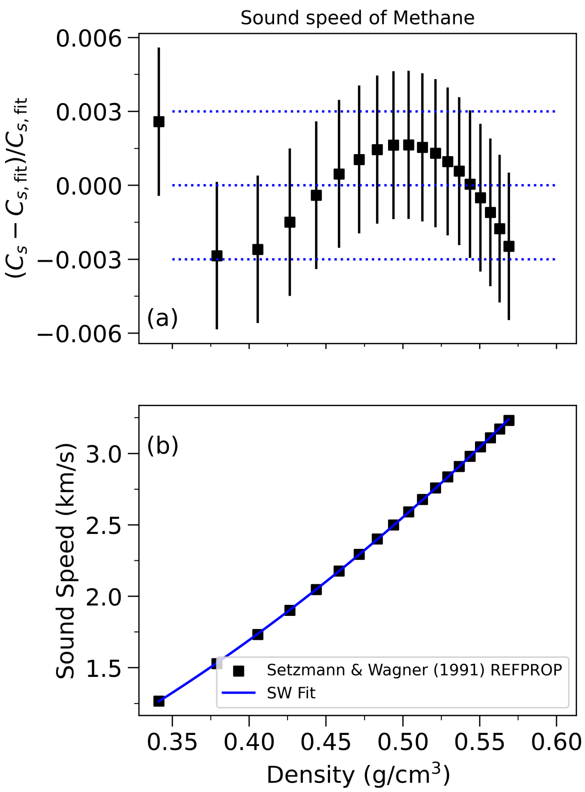

FIG. 7. Sound speed fit for methane based on REFPROP [36, 37]. (a) Deviation of REFPROP points (black) from fit (blue, with error envelope). (b) Methane density vs. sound speed.

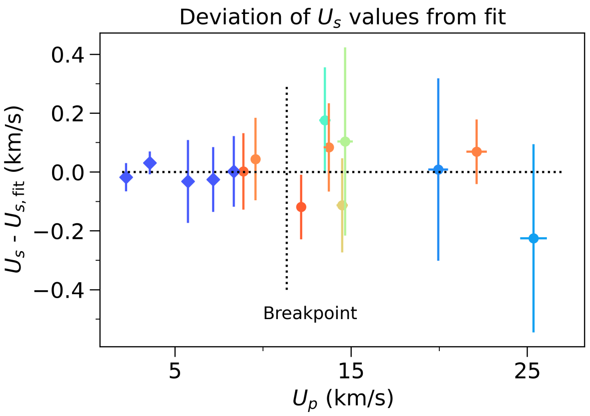

FIG. 8. Deviation of measured shock velocities from Hugoniot fit (Equation (3)). The data from this work are fit together with the prior gas-gun experiments [15]. The breakpoint was determined by imposing continuity on the fit.

[1] M. Ross, Nature **292**, 435 (1981).

[2] W. B. Hubbard, Science **214**, 145 (1981).

[3] W. B. Hubbard, W. J. Nellis, A. C. Mitchell, N. C. Holmes, S. S. Limaye, and P. C. McCandless, Science **253**, 648 (1991).

[4] D. S. Spiegel, J. J. Fortney, and C. Sotin, Proc. Natl. Acad. Sci. U.S.A. **111**, 12622 (2014).

[5] M. A. Barrios, D. G. Hicks, T. R. Boehly, D. E. Fratanduono, J. H. Eggert, P. M. Celliers, G. W. Collins, and D. D. Meyerhofer, Phys. Plasmas **17**, 056307 (2010).

[6] L. Sun, W. Yi, L. Wang, J. Shu, S. Sinogeikin, Y. Meng, G. Shen, L. Bai, Y. Li, J. Liu, H. kwang Mao, and W. L. Mao, Chem. Phys. Lett. **473**, 72 (2009).

[7] L. J. Conway and A. Hermann, Geosciences **9**, 10.3390/geosciences9050227 (2019).

[8] G. Gao, A. R. Oganov, Y. Ma, H. Wang, P. Li, Y. Li, T. Iitaka, and G. Zou, J. Chem. Phys. **133**, 144508 (2010).

[9] F. Ancilotto, G. L. Chiarotti, S. Scandolo, and E. Tosatti, Science **275**, 1288 (1997).

[10] B. L. Sherman, H. F. Wilson, D. Weeraratne, and B. Militzer, Phys. Rev. B **86**, 224113 (2012).

[11] G. Cheng, S. Hamel, and M. Bethkenhagen, Nat. Commun. **14**, 1104 (2023).

[12] L. R. Benedetti, J. H. Nguyen, W. A. Caldwell, H. Liu, M. Kruger, and R. Jeanloz, Science **286**, 100 (1999).

[13] H. Hirai, K. Konagai, T. Kawamura, Y. Yamamoto, and T. Yagi, Phys. Earth Planet. Inter. **174**, 242 (2009), advances in High Pressure Mineral Physics: from Deep Mantle to the Core.

[14] M. L. Elert, S. V. Zybin, and C. T. White, J. Chem. Phys. **118**, 9795 (2003).

[15] W. J. Nellis, F. H. Ree, M. van Thiel, and A. C. Mitchell, J. Chem. Phys. **75**, 3055 (1981).

[16] W. J. Nellis, D. C. Hamilton, and A. C. Mitchell, J. Chem. Phys. **115**, 1015 (2001).

[17] S. Zhang, B. Militzer, L. X. Benedict, F. Soubiran, P. A. Sterne, and K. P. Driver, J. Chem. Phys. **148**, 102318 (2018).

[18] S. Zhang, K. P. Driver, F. m. c. Soubiran, and B. Militzer, Phys. Rev. E **96**, 013204 (2017).

[19] P. Loubeyre, P. M. Celliers, D. G. Hicks, E. Henry, A. Dewaele, J. Pasley, J. Eggert, M. Koenig, F. Occelli, K. M. Lee, R. Jeanloz, D. Neely, A. Benuzzi-Mounaix, D. Bradley, M. Bastea, S. Moon, and G. W. Collins, High Press. Res. **24**, 25 (2004).

[20] P. Loubeyre, S. Brygoo, J. Eggert, P. M. Celliers, D. K. Spaulding, J. R. Rygg, T. R. Boehly, G. W. Collins, and R. Jeanloz, Phys. Rev. B **86**, 144115 (2012).

[21] J. Eggert, S. Brygoo, P. Loubeyre, R. S. McWilliams, P. M. Celliers, D. G. Hicks, T. R. Boehly, R. Jeanloz, and G. W. Collins, Phys. Rev. Lett. **100**, 124503 (2008).

[22] P. M. Celliers, P. Loubeyre, J. H. Eggert, S. Brygoo, R. S. McWilliams, D. G. Hicks, T. R. Boehly, R. Jeanloz, and G. W. Collins, Phys. Rev. Lett. **104**, 184503 (2010).

[23] M. Millot, S. Hamel, J. R. Rygg, P. M. Celliers, G. W. Collins, F. Coppari, D. E. Fratanduono, R. Jeanloz, D. Swift, and J. H. Eggert, Nat. Phys. **14**, 297 (2018).

[24] S. Brygoo, M. Millot, P. Loubeyre, A. E. Lazicki, S. Hamel, T. Qi, P. M. Celliers, F. Coppari, J. H. Eggert, D. E. Fratanduono, D. G. Hicks, J. R. Rygg, R. F. Smith, D. C. Swift, G. W. Collins, and R. Jeanloz, J. Appl. Phys. **118**, 195901 (2015).

[25] L. E. Crandall, J. R. Rygg, D. K. Spaulding, T. R. Boehly, S. Brygoo, P. M. Celliers, J. H. Eggert, D. E. Fratanduono, B. J. Henderson, M. F. Huff, R. Jeanloz, A. Lazicki, M. C. Marshall, D. N. Polsin, M. Zaghoo, M. Millot, and G. W. Collins, Phys. Rev. Lett. **125**, 165701 (2020).

[26] L. E. Crandall, J. R. Rygg, D. K. Spaulding, M. F. Huff, M. C. Marshall, D. N. Polsin, R. Jeanloz, T. R. Boehly, M. Zaghoo, B. J. Henderson, S. Brygoo, P. M. Celliers, J. H. Eggert, D. E. Fratanduono, A. Lazicki, M. Millot, and G. W. Collins, Phys. Plasmas **28**, 022708 (2021).

[27] Y.-J. Kim, B. Militzer, B. Boates, S. Bonev, P. M. Celliers, G. W. Collins, K. P. Driver, D. E. Fratanduono, S. Hamel, R. Jeanloz, J. R. Rygg, D. C. Swift, J. H. Eggert, and M. Millot, Phys. Rev. Lett. **129**, 015701 (2022).

[28] S. Brygoo, P. Loubeyre, M. Millot, J. R. Rygg, P. M. Celliers, J. H. Eggert, R. Jeanloz, and G. W. Collins, Nature **593**, 517 (2021).

[29] D. G. Hicks, T. R. Boehly, P. M. Celliers, J. H. Eggert, E. Vianello, D. D. Meyerhofer, and G. W. Collins, Phys. Plasmas **12**, 082702 (2005).

[30] D. G. Hicks, T. R. Boehly, J. H. Eggert, J. E. Miller, P. M. Celliers, and G. W. Collins, Phys. Rev. Lett. **97**, 025502 (2006).

[31] M. D. Knudson and M. P. Desjarlais, Phys. Rev. B **88**, 184107 (2013).

[32] M. P. Desjarlais, M. D. Knudson, and K. R. Cochrane, J. Appl. Phys. **122**, 035903 (2017).

[33] A. D. Chijioke, W. J. Nellis, A. Soldatov, and I. F. Silvera, J. Appl. Phys. **98**, 114905 (2005).

[34] A. Dewaele, J. H. Eggert, P. Loubeyre, and R. Le Toullec, Phys. Rev. B **67**, 094112 (2003).

[35] Y.-J. Kim, P. M. Celliers, J. H. Eggert, A. Lazicki, and M. Millot, Sci. Rep. **11**, 5610 (2021).

[36] U. Setzmann and W. Wagner, J. Phys. Chem. Ref. Data **20**, 1061 (1991).

[37] M. L. Huber, E. W. Lemmon, I. H. Bell, and M. O. McLinden, Ind. Eng. Chem. Res. **61**, 15449 (2022).

[38] P. Kortbeek and J. Schouten, Int. J. Thermophys. **11**, 455 (1990).

[39] J. D. Olson, J. Chem. Phys. **63**, 474 (1975).

[40] M. Li, F. Li, W. Gao, C. Ma, L. Huang, Q. Zhou, and Q. Cui, J. Chem. Phys. **133**, 044503 (2010).

[41] H. Shimizu, N. Nakashima, and S. Sasaki, Phys. Rev. B **53**, 111 (1996).

[42] P. M. Celliers, D. K. Bradley, G. W. Collins, D. G. Hicks, T. R. Boehly, and W. J. Armstrong, Rev. Sci. Instrum. **75**, 4916 (2004).

[43] P. M. Celliers and M. Millot, Rev. Sci. Instrum. **94**, 011101 (2023).

[44] M. Millot, P. M. Celliers, P. A. Sterne, L. X. Benedict, A. A. Correa, S. Hamel, S. J. Ali, K. L. Baker, L. F. Berzak Hopkins, J. Biener, G. W. Collins, F. Coppari, L. Divol, A. Fernandez-Panella, D. E. Fratanduono, S. W. Haan, S. Le Pape, N. B. Meezan, A. S. Moore, J. D. Moody, J. E. Ralph, J. S. Ross, J. R. Rygg, C. Thomas, D. P. Turnbull, C. Wild, and J. H. Eggert, Phys. Rev. B **97**, 144108 (2018).

[45] Y. B. Zel'dovich and Y. P. Raizer, *Physics of Shock Waves and High-Temperature Hydrodynamic Phenomena* (Dover Publications, 2002).

[46] I. P. Dudoladov, V. I. Rakitin, Y. N. Sutulov, and G. S. Telegin, J. Appl. Mech. Tech. Phys. **10**, 673 (1969).

[47] R. G. McQueen, S. P. Marsh, J. W. Taylor, J. N. Fritz, and W. J. Carter, in *High Velocity Impact Phenomena*, edited by R. Kinslow (Academic Press, New York, 1970) pp. 293–417.

[48] M. Van Thiel, J. Shaner, and E. Salinas, *Compendium of Shock Wave Data*, Tech. Rep. (Lawrence Livermore National Laboratory, 1977).

[49] S. P. Marsh, *LASL Shock Hugoniot Data* (University of California Press, 1980).

[50] B. Militzer, F. Gonzá lez-Cataldo, S. Zhang, K. P. Driver, and F. Soubiran, Phys. Rev. E **103**, 10.1103/physreve.103.013203 (2021).

[51] G. I. Kerley, J. Appl. Phys. **51**, 5368 (1980).

[52] B. Ruscic, J. Phys. Chem. A **119**, 7810 (2015), pMID: 25760799.